Chapter 6

Magnetic Resonance Imaging

Authors: Felix Lugauer and Jens Wetzl

Modern MRI systems allow physicians to look inside the body without the use of ionizing radiation (see Fig. 6.1). They provide excellent soft-tissue contrast for morphological imaging as well as a range of possibilities for functional imaging, e. g., for visualizing blood flow, tissue perfusion or diffusion processes. In the following chapter, we will outline the physical fundamentals of magnetic resonance (MR), concepts for imaging, common pulse sequences to produce different contrasts as well as some advanced topics related to speeding up the acquisition and for functional imaging.

6.1 Nuclear Magnetic Resonance (NMR)

6.1.1 Genesis of the Resonance Effect

To explain the MR effect, we first look at the example of a compass needle which is subjected to a magnetic field. The needle progressively aligns itself along the direction of the magnetic field by oscillating around it, as shown in Fig. 6.2. The amplitude of the oscillation decreases over time. But the

A. Maier et al. (Eds.): Medical Imaging Systems, LNCS 11111, pp. 91–118, 2018.
https://doi.org/10.1007/978-3-319-96520-8_6

Figure 6.1: A modern MRI scanner can provide both morphological and functional imaging. Image courtesy of Siemens Healthineers AG.

frequency of the oscillation is determined by the strength of the magnetic field and the properties of the needle and remains fixed over time.

Now recall that a radio frequency (RF) wave corresponds to a magnetic field that varies over time. So during its oscillation, our magnetic needle can be seen as an antenna that emits RF waves at the frequency of its oscillation. These emissions stop once the needle has reached a stable position, but by pushing it out of balance, we can cause new RF waves to be emitted. This "push" can also be achieved by means of a magnetic field, one that is applied perpendicularly to the original magnetic field which the needle is aligned with. A Java applet[1] can simulate this process. Broadly speaking, this is the same principle that is applied in MRI to generate images.

The "magnetic needles" in our body commonly used for MRI are hydrogen (^{1}H) nuclei. They have an intrinsic property known as *spin*, visualized as the rotation of a sphere around an axis in Fig. 6.3, which makes them act like small magnets. The endpoints of the axis of rotation can be thought of as the poles of the magnetic needle. In the absence of an external magnetic field, the axes of hydrogen nuclei within the body are randomly distributed, so the sum of all magnetic fields is zero. Subjected to a large magnetic field, denoted by $\boldsymbol{B}_0$, spin axes have the tendency to align in the direction of the magnetic field, similarly to the compass needles. In contrast to a compass, this alignment is only partial, due to random interactions between nuclei (compare Fig. 6.4). Even so, the sum of all spin directions no longer cancels out and will instead point in the direction of the magnetic field. In what follows, we will call this sum of all spin directions the *net (total) magnetization vector* $\boldsymbol{M}$.

Thus, the nuclei inside the body will accumulate to a net magnetization in the presence of a strong magnetic field $\boldsymbol{B}_0$ as the partially aligned spin

[1] http://drcmr.dk/JavaCompass/

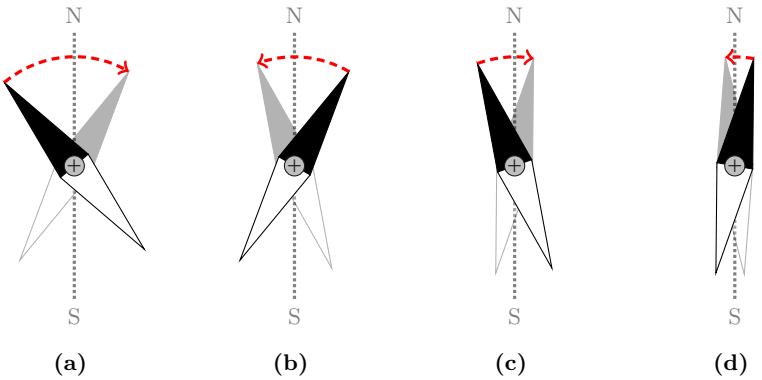

Figure 6.2: Behavior of a compass needle in a magnetic field. The needle oscillates through the "north" position until it reaches a stable position. In real compasses, the magnetic needle is immersed in a fluid to dampen such oscillations.

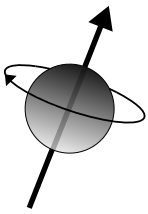

Figure 6.3: Hydrogen nuclei are used for MRI because of their magnetic susceptibility and their vast amount in the human body. An intrinsic property of the hydrogen nuclei is their rotation (spin) which makes them magnetic along the rotational axis.

axes sum up to $\boldsymbol{M}$. Applying, for instance, a field strength of 1 T (tesla) to a million nuclei yields a net magnetization with the magnetic strength of about 3 nuclei, which means that one million partially aligned nuclei make up for only 3 completely aligned nuclei. The induced magnetization $\boldsymbol{M}$ is proportional to the applied field strength of $\boldsymbol{B}_0$ and as there are over 10^{27} hydrogen nuclei in the whole body, the net magnetization accumulates to a measurable magnitude.

In our compass example, we said that the magnetic needle oscillates until it reaches a stable position, and emits RF waves due to this oscillation. The oscillation of the needle is a 2-dimensional motion happening in the plane of the compass. For spin axes, a similar process happens, but the motion is 3-dimensional and is called *precession*. From its initial position, the spin axis rotates around the axis of the strong magnetic field $\boldsymbol{B}_0$. At the same time, the angle between the spin axis and $\boldsymbol{B}_0$ decreases over time, until they are

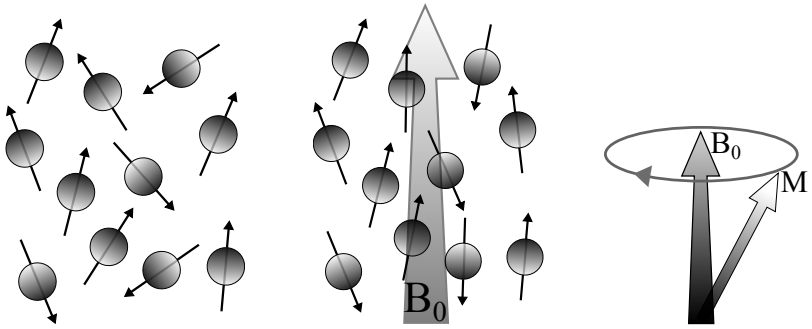

(a) Random spins **(b)** Partially aligned spins **(c)** Precession

Figure 6.4: Nuclei axes within the body will point randomly (a) until a strong magnetic field forces their rotation axes to partially align with the applied magnetic field (b). The accumulated magnetization of all spins $\boldsymbol{M}$ precesses around $\boldsymbol{B}_0$ (c).

aligned. The same motion can be observed in reverse with a spinning top, with the spin axis corresponding to the tilt of the spinning top and the axis of $\boldsymbol{B}_0$ corresponding to the direction of gravity[2]. As with the oscillation of the compass needle, the precession causes the emission of RF waves.

We said for the magnetic needle that the frequency of the oscillation is determined by the strength of the magnetic field and the properties of the needle and that it remains fixed over time. The same holds for nuclear spin precession, and the frequency of the precession is

$$f_\ell = \gamma \cdot \|\boldsymbol{B}_0\|, \tag{6.1}$$

also known as the *Larmor frequency*. The *gyromagnetic ratio* γ is the field strength dependent ratio for a specific nucleus, which is 42.576 MHz/T for hydrogen. Using, for instance, a 1.5 T field strength, protons will resonate with a frequency of about 64 MHz. Please note that precession should not be confused with spin, being the rotation of a single nucleus around its own axis.

We will now abstract away from the behavior of individual spins and only consider the net magnetization $\boldsymbol{M}$. Analogously to our compass needle, we will push $\boldsymbol{M}$ out of its stable position, a process which we call *excitation*, to cause the emission of RF waves from the body. The direction of $\boldsymbol{M}$ can be modified through a weaker magnetic field $\boldsymbol{B}_1$ in a direction orthogonal to $\boldsymbol{B}_0$ by applying RF waves from a coil in the resonance frequency of $\boldsymbol{M}$.

In the case of $\boldsymbol{M}$, this is not as straightforward as it was for the compass needle. In the 2-D plane of the compass, there is only one choice for the direc-

[2] MIT Physics Demo: https://www.youtube.com/watch?reload=9&v=8H98BgRzpOM

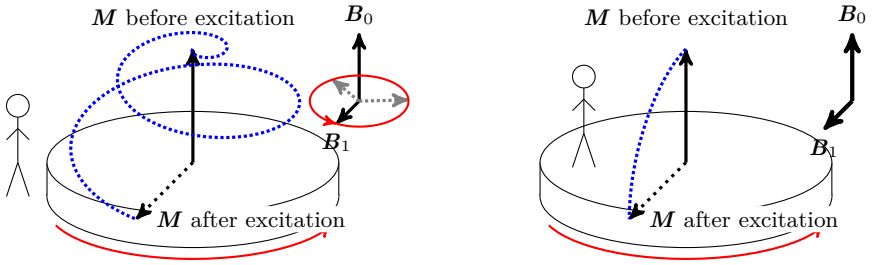

(a) "World" frame of reference **(b)** Rotating frame of reference

Figure 6.5: Excitation of the magnetization vector $\boldsymbol{M}$ viewed from the world (a) and rotating frame of reference (b). The precession is illustrated as a turntable, denoted by the red arrow, on which $\boldsymbol{M}$ is mounted. Viewed from the outside, the combination of the precession and excitation motions looks quite complex and the $\boldsymbol{B}_1$ field rotates in tune to the precession. From the rotating frame of reference, only the simple path of the excitation motion is visible and the $\boldsymbol{B}_1$ field is static. Figure recreated from [9].

tion of the second magnetic field, which is orthogonal to the main magnetic field. $\boldsymbol{M}$ precesses in a 3-D motion around $\boldsymbol{B}_0$, so the second magnetic field $\boldsymbol{B}_1$ must be orthogonal to $\boldsymbol{B}_0$ as well as aligned with the current rotation angle of $\boldsymbol{M}$. But we can simplify things if we change our point of view. Imagine the precession of $\boldsymbol{M}$ by picturing that the vector $\boldsymbol{M}$ is "attached" to a turntable which is rotating around $\boldsymbol{B}_0$. The motion of $\boldsymbol{M}$ as it is being pushed out of balance and precessing at the same time seems complicated, as does the direction of $\boldsymbol{B}_1$ that needs to be applied, see Fig. 6.5(a). Now if we step onto the turntable and look at the motion again, it is much simpler. In this *rotating frame of reference*, the direction of $\boldsymbol{B}_1$ is constant, and we cannot see the precession motion, only the excitation caused by $\boldsymbol{B}_1$, see Fig. 6.5(b).

Once the secondary magnetic field $\boldsymbol{B}_1$ is turned off, the magnetization vector $\boldsymbol{M}$ will slowly return to the equilibrium position by a process called *relaxation*, which is described in the next subsection. During this process, RF waves are emitted from the body and can be received with coils placed near the body surface. This is the signal from which MR images are then generated, as outlined in Sec. 6.2.

6.1.2 Relaxation and Contrasts

This section aims at explaining the concept of relaxation, which is the origin of contrast between different tissues in the resulting images. Relaxation is the process that causes the net magnetization to constantly approach equilibrium,

i. e., resting state again after excitation by an RF pulse. In addition to the dependency on the field strength, the speed of relaxation is tissue dependent as proton interactions are limited for large molecules or dense tissue where water molecule movement is hindered. This means that different tissue, e. g., water and fat, will end relaxation at different time points and, thus, the amount of signal received during relaxation time will differ. This is what gives rise to the contrast between tissue in MR images. To differentiate between different tissues, we will no longer look at the net magnetization vector $\boldsymbol{M}$ of all excited spins but instead overlay our imaging volume with a voxel grid and look at magnetization vectors per voxel.

6.1.2.1 Relaxation

Let's first recap the situation before relaxation starts: The per-voxel magnetization vectors are initially aligned with the main magnetic field $\boldsymbol{B}_0$, which we will now assume to be aligned with the z axis of our coordinate system. As such, each magnetization vector can be split into a *longitudinal* component $\boldsymbol{M}_z$ and a *transversal* component $\boldsymbol{M}_{xy}$ such that $\boldsymbol{M} = \boldsymbol{M}_{xy} + \boldsymbol{M}_z$. So initially, $\|\boldsymbol{M}_{xy}\| = 0$ and $\|\boldsymbol{M}_z\|$ is a positive number dependent on the number of hydrogen nuclei contained within the voxel. During excitation, an RF pulse tips the magnetization vector into the transversal plane, such that $\|\boldsymbol{M}_z\| = 0$ and $\|\boldsymbol{M}_{xy}\|$ is maximal. We call such an RF wave a *90° pulse* because it changes the angle of the magnetization vector by 90°.

Once the 90° pulse ends, relaxation occurs in the form of two independent processes to get back to the equilibrium state. The magnetization vector recovers its longitudinal component, i. e., $\|\boldsymbol{M}_z\|$ tends towards its original magnitude. And, usually much faster, the magnetization vector loses its transversal component, i. e., $\|\boldsymbol{M}_{xy}\|$ tends towards 0. These independent processes happen on different time scales, meaning that the magnitude of the magnetization vector is not constant over time. Fig. 6.6 visualizes the trajectory of a magnetization vector during relaxation. The physical reasons for both relaxation processes are outlined in the following paragraphs.

Recovery of longitudinal magnetization

is achieved by a process called spin-lattice relaxation, whereby the nuclear spins release the energy received from an RF pulse back into the surrounding lattice (tissue), leading towards thermal equilibrium or resting state. The recovery of the longitudinal magnetization follows an exponential function $\|\boldsymbol{M}_z(t)\| = \|\boldsymbol{M}_0\|(1 - \mathrm{e}^{-t/T_1})$, which is characterized by a time constant T_1, which is different for each tissue class. The time constant T_1 is defined as time period for $\boldsymbol{M}_z$ to recover $1 - \frac{1}{\mathrm{e}} \approx 63\,\%$ of its initial magnetization $\boldsymbol{M}_0$. This characteristic number of an exponential function serves to determine the

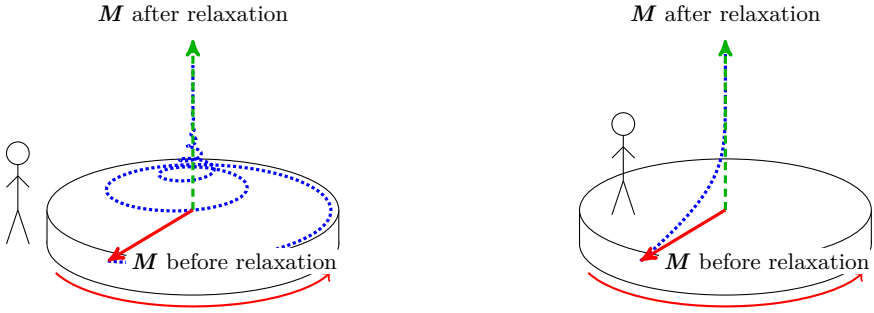

(a) "World" frame of reference

(b) Rotating frame of reference

Figure 6.6: Visualization of the precession and relaxation of white matter with $T_1 = 510\,\text{ms}$ and $T_2 = 67\,\text{ms}$ in the "world" (a) and rotating frame of reference (b). After 90° RF excitation, the magnetization is in the transverse plane (red vector), which is the starting point for the relaxation process. The magnetization then follows the blue trajectory until the resting state (green vector) is reached. Figure recreated and amended from [9].

point in time when the process is considered "finished". The common wisdom is that after $5T_1$, which corresponds to a 99.3 % recovery, the process is as good as done. As an example, white matter has a T_1 of 510 ms while it is 2500 ms for arterial blood. The magnetization recovery for arterial blood is plotted in Fig. 6.7(a).

Decay of transversal magnetization (in theory)

The decay of transversal magnetization is caused by random interactions between nuclei when a perfectly homogenous magnetic field can be assumed. More explicitly, interactions between the magnetic fields of nuclei lead to temporary phase differences. Ultimately, the nuclei move out-of-phase and the overall signal that can be measured along $\boldsymbol{B}_1$ decreases affecting the transversal magnetization $\boldsymbol{M}_{xy}$. Again, the magnetization is an exponential function but this time the exponential time constant T_2 determines the *decay* of $\|\boldsymbol{M}_{xy}(t)\| = \|\boldsymbol{M}_0\|\mathrm{e}^{-t/T_2}$. T_2 is defined as the time after excitation when the signal value is decreased to $\frac{1}{\mathrm{e}} \approx 37\,\%$ of its initial value $\boldsymbol{M}_0$. It is dependent on the tissue density or rather the chemical structure, and, thereby, also characteristic for every tissue. The longitudinal magnetization decay of arterial blood is plotted in Fig. 6.7(b).

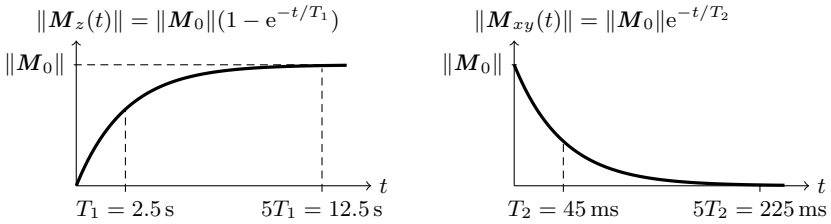

(a) Longitudinal magnetization recovery **(b)** Transverse magnetization decay

Figure 6.7: Plots of the recovery of longitudinal magnetization (a) and the decay of transverse magnetization (b) for arterial blood with $T_1 = 2.5\,\mathrm{s}$ and $T_2 = 45\,\mathrm{ms}$. As a rule of thumb, the process is considered completed after five times the respective time constant, with over 99 % of the longitudinal magnetization restored after $5T_1$ and less than 1 % of transverse magnetization remaining after $5T_2$.

Decay of transversal magnetization (in practice)

The actual decay happens more quickly, i. e., the received signal in an MRI acquisition decays faster than predicted by T_2. This is due to imperfections in the homogeneity of the main magnetic field $\boldsymbol{B}_0$, which is related to various effects like magnetic susceptibilities and magnet manufacture. T_2^* („T two star“) refers to the relaxation which includes the ideal tissue-dependent relaxation due to random interactions between nuclei (T_2) plus the additional loss of signal due to field imperfections. Note that T_2^* is also affected by tissue-dependent magnetic susceptibilities and is always shorter than T_2. However, there exists a measurement method, called *spin echo* that can recover the signal lost through field dependent dephasing of nuclei via refocusing pulses (see Sec. 6.3.1).

Fig. 6.7 compares the exponential course of T_1 recovery and T_2 decay, produced by the signal of arterial blood. Now, we can also fully explain the 3-D visualization of relaxation in Fig. 6.6 which is described by the blue trajectory: the net magnetization vector $\boldsymbol{M}_0$ (green) has been completely tipped into the xy-plane (red vector). As relaxation starts, imagine the length of the red vector to decrease ($\boldsymbol{M}_{xy}$) with an exponential decay defined by T_2, while at the same time the length of the green vector ($\boldsymbol{M}_{xy}$) grows with a speed defined by T_1. Above all, the magnetization vector rotates around the main magnetic field $\boldsymbol{B}_0$ (here, z-direction) with the field strength dependent Larmor frequency.

6.1.2.2 Contrasts

MR images can be controlled by a large number of parameters including the type of sequence and numerous sequence parameters per acquisition. The choice of the contrast or weighting for a particular image is fundamental as it determines the subsequent medical application and hereby its diagnostic significance. There are three major contrasts being distinguished: T_1 weighting, T_2 weighting and proton density (PD) weighting. Weighting is used in the sense that the acquisition parameters were chosen such that image contrast mainly reflects variations due to one of these tissue-inherent properties, for instance, spin-spin relaxation (T_2).

The parameters that control the particular weighting of a spin echo sequence are the *echo time (TE)* and the *repetition time (TR)*. TE is the time delay after an emitted RF pulse until the RF signal is measured. In the meantime, transversal magnetization decay and signal loss will occur due to T_2 relaxation, which means that the TE determines the T_2 weighting of images. For example, a long TE compared to the T_2 of the tissue being captured yields a strong T_2 contrast but only little signal as the signal decay has progressed for a long time.

TR is the period of time between successive RF pulses. Several similar measurements are needed, for instance, to encode multiple lines per image or for advanced imaging protocols. An RF pulse in succession will flip parts of the *available* longitudinal magnetization into the transversal plane. During the following relaxation, the longitudinal magnetization builds up again with a speed determined by T_1. If the time between successive measurement is short (short TR), the available magnetization is used often and cannot recover to equilibrium yielding a relatively small signal per repetition. A long TR, in contrast, will produce a stronger signal as most of the longitudinal magnetization will have recovered by then. However, the contrast in T_1 vanishes entirely if the longitudinal magnetization has fully recovered before the measurement is taken, i. e., TR is significantly longer than T_1 of the tissues. Thus, the T_1 weighting of an image is controlled by TR where a long TR produces a signal-intense limited T_1 weighting and a short TR will amplify the variations between tissue with varying T_1 but with a generally weak signal.

The third type of contrast, proton density weighting, is chosen to minimize both T_1 and T_2 variations. What is then left are variations due to the proton density itself, a tissue specific property which quantifies the number of mobile hydrogen protons per unit volume. As the number of mobile hydrogens bound in water decreases slightly from pure water over fat to solids, a PD-weighted image allows to enhance these variations. A long TR, sufficient for the magnetization to recover to equilibrium state, in combination with a short TE leads to a proton density weighted image. In summary, the following applies for sequences that consist of a simple excite-wait-measure-wait scheme:

	short TE	**long TE**
short TR	T_1 weighting	—
long TR	PD weighting	T_2 weighting

T_1 weighting is determined by a *short* TE to minimize T_2 effects and a *short* TR ($\sim T_1$) at which the longitudinal magnetization has not yet recovered.

T_2 weighting can be achieved by a *long* TR to reduce T_1 impact and a *long* TE ($\sim T_2$) to allow the differences in T_2 decay to appear.

PD weighting is given by a *long* TR such that the magnetization can reach equilibrium and measured immediately after the RF pulse (*short* TE).

The missing combination is long TE and short TR, which would result in a contrast mixture of T_1 and T_2 with no clinical use and, additionally, a weak signal amplitude.

6.2 Principles of Magnetic Resonance Imaging

Having introduced the underlying physical phenomenon of MR, we will now look at the *imaging* component of MRI. So far, we cannot localize the source of an emitted radio frequency wave, but only measure the sum of the signals from all spatial locations affected by an excitation.

An important component of an MRI system are the gradient coils, which allow us to impose a linear variation of the otherwise homogeneous magnetic field $\boldsymbol{B}_0$. Three gradient coils oriented in three orthogonal directions, e. g., head-feet, left-right and anterior-posterior, enable such a variation in any spatial direction by a weighted combination of the three.

Two concepts based on the gradient coil system will be explained to allow the spatial localization of emitted RF waves: slice selection and spatial encoding.

6.2.1 Slice Selection

An intuitively understood concept is that of slice-selective excitation. If the gradient coils are used to induce a linear variation of the main magnetic field $\boldsymbol{B}_0$ in head-feet direction, then the Larmor frequency f_ℓ of hydrogen nuclei – where resonance occurs – will be spatially dependent on their offset z along the direction:

$$f_\ell(z) = \gamma \cdot (\|\boldsymbol{B}_0\| + z) \tag{6.2}$$

Depending on the direction of the linear gradient, the Larmor frequency for ^{1}H nuclei in the feet would be lower or higher than that of nuclei in the

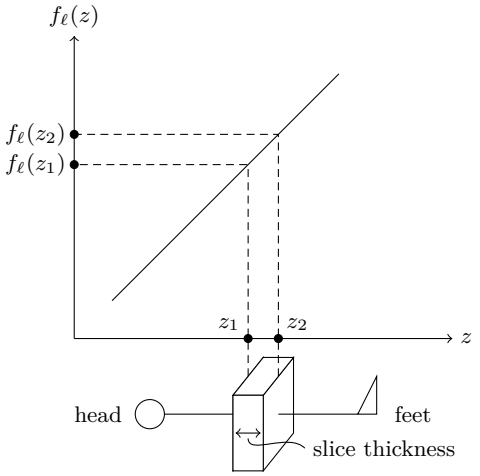

Figure 6.8: A linear variation of the magnetic field in head-feet direction causes the Larmor frequency $f_\ell(z)$ to be spatially dependent on the offset z along the variation direction. An excitation pulse with frequencies in the range of $f_\ell(z_1)$ to $f_\ell(z_2)$ will cause resonance in nuclei that lie within the depicted slice of thickness $|z_1 - z_2|$.

head. Now modifying the frequency of the excitation RF wave allows a slice-selective excitation, only nuclei whose Larmor frequency matches that of the wave will be excited.

If the excitation contains only a single frequency, the corresponding excited slice will be infinitely thin and not enough nuclei will resonate to produce a measurable signal. By emitting a wave containing a range of frequencies, the thickness of a slice can be chosen to provide a good trade-off between spatial resolution and signal-to-noise ratio. A visualization of this concept is shown in Fig. 6.8.

6.2.2 Spatial Encoding

Unfortunately, the slice selection method cannot be extended to encode spatial locations within a slice. Even with multiple gradient fields, we can only select a (possibly oblique) plane, not a single point in 3-D space. Instead, we make use of the phase information of spins in the transversal plane, i. e., the direction they are pointing.

6.2.2.1 One-dimensional Example

We will illustrate this with a 1-D example "image" and later extend the concept to multiple dimensions. Within our example slice, there are more hydrogen nuclei toward the boundaries and less in the middle, represented by the magnitude of the magnetization vectors within each voxel.

Directly after excitation, all spins within the excited slice point in the same direction. The quantity measurable by our MRI system is the net magnetization, the sum of all spin magnetization vectors within the voxels of the excited slice:

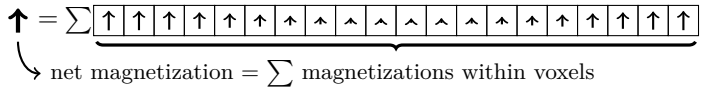

In the absence of any relaxation, all spins would precess at the Larmor frequency implied by the magnetic field strength. Assuming a homogeneous magnetic field, the magnitude of the net magnetization vector would not change:

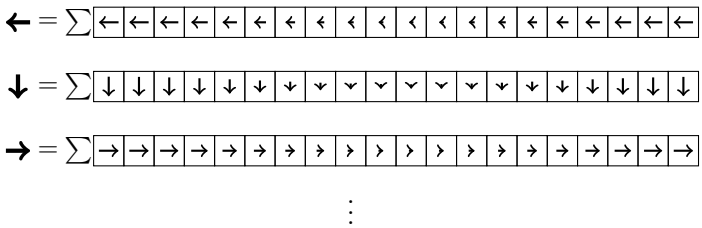

By applying a linear gradient, the precession frequency of spins changes along the direction of the gradient, i. e., spins to the right rotate faster than those on the left. Spins are no longer *in phase*, and the phase shift between adjacent voxels is dependent on the strength of the applied field. This phase shift has an influence on the magnitude of the net magnetization vector and it may even become zero. A graph of the net magnetization magnitude for different gradient field strengths is shown below, with two example "images" showing different phase shifts.

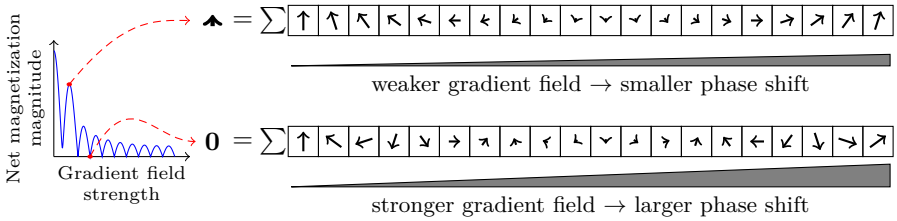

This may seem counterproductive at first sight, but it is the core principle of spatial encoding. If the hydrogen nuclei distribution of the measured tissue matches the "pattern" implied by the phase shift, there will be a measurable net magnetization. The better the match, the higher the magnitude of the net magnetization will be, as shown here:

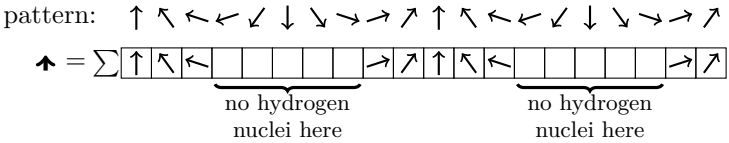

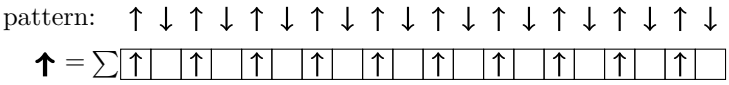

So by applying different gradients, i. e., creating different patterns in the phase orientation of spins, and measuring the net magnetization, i. e., the similarity to the applied pattern, we can get an intermediate representation of the underlying hydrogen density distribution. If done properly, the actual distribution within a slice can then be reconstructed from this intermediate representation. Note that this step happens after slice selection, i. e., the phase encoding is only applied to spins within the slice of interest.

The phase pattern can also be understood in terms of an intensity pattern, by mapping phase angles to gray values. For the two phase patterns shown above, the corresponding intensity patterns are shown here:

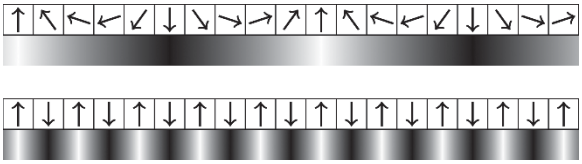

The observations above can also be derived mathematically and demonstrate that we are actually measuring the Fourier transform of the signal (cf. Geek Box 6.1).

Geek Box 6.1: Relation to 1-D Fourier Transform

The phase pattern can be described as a function which maps the offset in right-left direction x to a complex number of magnitude 1 and an angle dependent on x and the phase shift k corresponding to the gradient field strength:

$$p_k(x) = \mathrm{e}^{\mathrm{i}kx} = \cos(kx) + \mathrm{i}\sin(kx) \tag{6.3}$$

The match of the pattern $p_k(x)$ to our image $f(x)$ is performed by a pointwise multiplication and summation, i. e., a correlation. The result is the measured net magnetization $m(k)$ dependent on the phase shift k:

$$m(k) = \int f(x)p_k(x)\ \mathrm{d}x \tag{6.4}$$

$$= \int f(x)\mathrm{e}^{\mathrm{i}kx}\ \mathrm{d}x \tag{6.5}$$

We can now see that the image $f(x)$ we want to compute is the Fourier transform of the measured net magnetization $m(k)$, which is how it can be reconstructed. In other words, phase encoding performs a Fourier decomposition of our image.

6.2.2.2 Generalization to Multiple Dimensions

The concept of phase encoding effortlessly generalizes to more dimensions. For example, to perform spatial localization in two dimensions within an excited slice, e. g., left-right and anterior-posterior, two gradient fields in those directions are applied to create 2-D phase patterns:

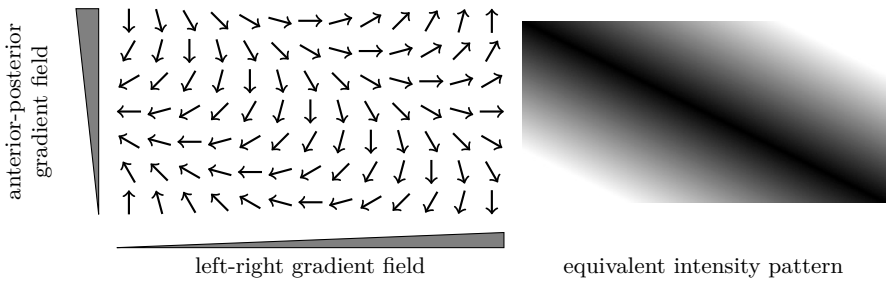

The concept can also be expanded to n-D and comprises again a Fourier transform (cf. Geek Box 6.2)

Geek Box 6.2: Relation to n-D Fourier Transform

In general, the phase shift pattern for an n-D image $f(\boldsymbol{x})$, $\boldsymbol{x} \in \mathbb{R}^n$, dependent on the phase shift in each dimension combined into a vector $\boldsymbol{k}$ is

$$p_{\boldsymbol{k}}(\boldsymbol{x}) = \mathrm{e}^{\mathrm{i}\langle \boldsymbol{x}, \boldsymbol{k} \rangle} = \cos\left(\sum_{j=1}^{n} x_j k_j\right) + \mathrm{i}\sin\left(\sum_{j=1}^{n} x_j k_j\right) \tag{6.6}$$

and the measured net magnetization $m(\boldsymbol{k})$ is the n-dimensional inverse Fourier transform of $f(\boldsymbol{x})$:

$$m(\boldsymbol{k}) = \int f(\boldsymbol{x}) p_{\boldsymbol{k}}(\boldsymbol{x}) \, \mathrm{d}\boldsymbol{x} \tag{6.7}$$

$$= \int f(\boldsymbol{x}) \mathrm{e}^{\mathrm{i}\langle \boldsymbol{x}, \boldsymbol{k} \rangle} \, \mathrm{d}\boldsymbol{x} \tag{6.8}$$

In the literature, a differentiation is often made, naming one of the considered dimensions the *frequency encoding direction* and the remaining $n-1$ dimensions the *phase encoding directions*. The process of spatial encoding is then explained as two separate steps, *frequency encoding* and *phase encoding*. However, the idea behind both is the same – the one outlined above – and the differences are only due to the technical procedure of reading out data with the scanner, which is omitted here.

6.2.3 *k*-space

In the magnetic resonance community, Fourier space is often referred to as $\boldsymbol{k}$-space as a reference to the wavenumber k. The purpose of an MRI examination is to fill the $\boldsymbol{k}$-space with data so that an image can be reconstructed from it. Fig. 6.9 shows an example for a 2-D $\boldsymbol{k}$-space with some associated phase patterns.

6.2.4 Slice-selective vs. Volume-selective 3-D Imaging

Having understood the concepts of slice selection and spatial encoding, two options present themselves for 3-D imaging:

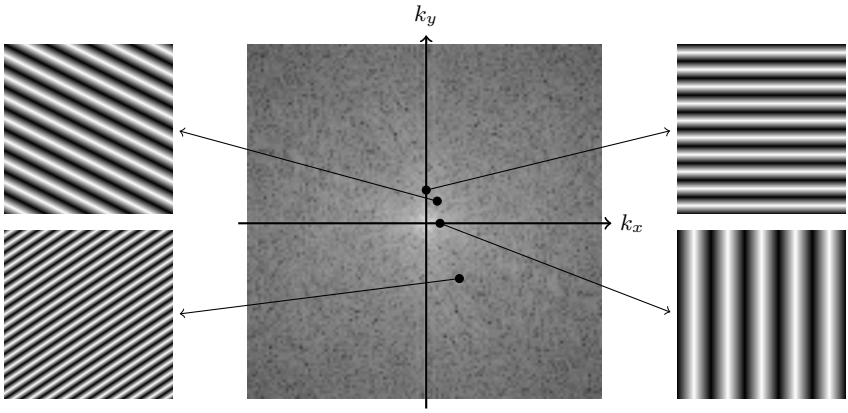

Figure 6.9: Example of a filled 2-D $\boldsymbol{k}$-space, with grey values encoding similarity as dark = low and bright = high, with associated phase patterns for some $\boldsymbol{k}$-space positions.

Slice-selective: Use slice selection to successively acquire, reconstruct, and stack 2-D slices of the desired 3-D volume, using 2-D spatial encoding for localization within each slice.

Volume-selective: Excite the entire volume without slice selection and use 3-D spatial encoding for localization, followed by a 3-D reconstruction.

Both approaches have advantages and disadvantages and the choice for which approach to use is dependent on the intended use of the acquired volume. Slice-selective acquisitions are commonly non-isotropic with high in-plane resolutions $< 1\,\text{mm}$, but with a high slice thickness of several millimeters. Volume-selective acquisitions have an inherent signal-to-noise ratio benefit because more ^{1}H nuclei resonate. They typically feature isotropic resolution which lies inbetween the in-plane resolution and slice thickness of slice-selective acquisitions (for comparable acquisition durations).

6.3 Pulse Sequences

A pulse sequence describes the sequence of RF pulses which are applied in repetition in order to successively acquire the whole $\boldsymbol{k}$-space of an object. This includes order and position of every sample as well as the information how the 3-D gradient coils of the scanner hardware have to be adjusted accordingly. Sequences can look quite complex in a detailed view but they are usually determined by a small number of recurring building blocks such as (partial) flips of longitudinal magnetization via RF excitations, waiting periods and readout gradients.

In the following, we focus on the description of the general concepts of two prominent pulse sequences.

6.3.1 Spin Echo

The spin echo (SE) pulse sequence is widely used as it allows to regain the signal loss due to field imperfections. As we discussed earlier in Sec. 6.1.2, the decay of transverse magnetization after excitation is subject to dephasing due to random interactions and external field inhomogeneities. Apparently, we cannot influence the random interactions between nuclei but we can alter the phase of nuclei using an 180° inversion pulse such that dephased nuclei can end up *in phase* again. For this to work, constant field imperfections are assumed which holds in practice for conventional MRI acquisitions. The principle of the spin echo sequence is shown in Fig. 6.10 and can be summarized to:

1. A 90° RF pulse flips the magnetization into the transversal plane.
2. Dephasing due to random nuclei interactions and field inhomogeneities sets in. Some nuclei will spin slightly faster and others slower due to local field variations. The phases of these nuclei will further diverge over time such that their magnetic moments will cancel each other, resulting in a decay of transversal magnetization.
3. After a waiting period of TE/2, a 180° pulse inverts the magnetization by flipping the dephased vectors along the x (or y) axis. In consequence, the nuclei whose phase trailed behind are now ahead of the main magnetic moment and vice versa.
4. After another waiting period of TE/2, all magnetic moments have refocused and are in phase again as the faster spins have caught up with the lower spinning nuclei by this time. Now, a large signal, so called *spin echo*, which is of negative sign but with the T_2^* effects removed can be measured.
5. Multiple echos can be formed by repeating steps 2–4 as long as some signal due to T_2 decay is available. Each signal has its own echo time TE_1, TE_2, ... after the 90° RF excitation.

6.3.2 Gradient Echo

The gradient echo (GRE) pulse sequence utilizes partial flips with angles below 90°, which allow for faster acquisitions compared to SE sequences. Note that the acquisition time for a single slice in a typical spin echo sequence is given by $\mathrm{TR} \cdot N_y \cdot N_{\mathrm{ex}}$, where N_y and N_{ex} are the number of phase encoding steps and excitations, respectively. As these parameters determine the result-

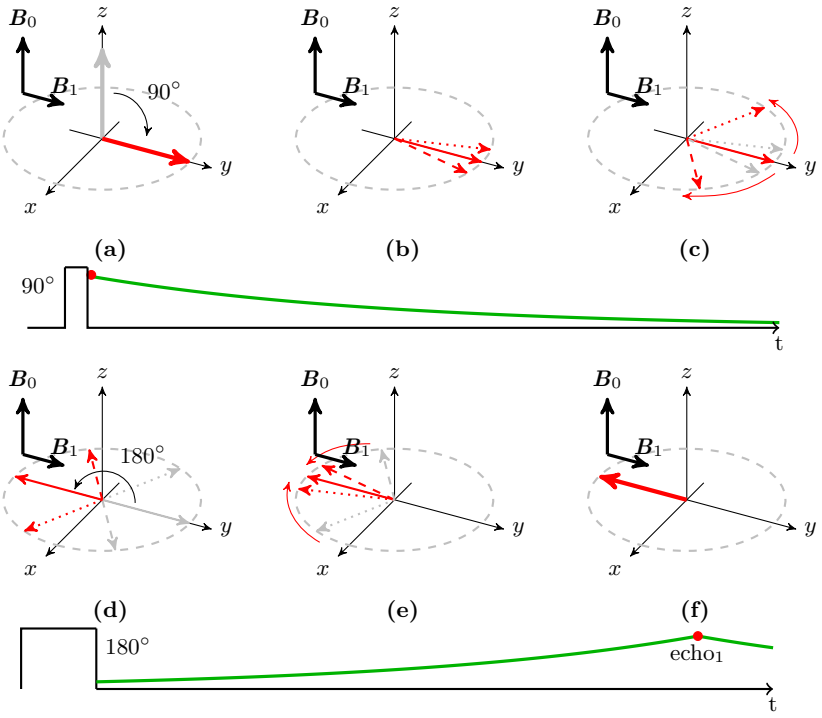

Figure 6.10: A 90° pulse tips the magnetization into the xy plane (a). Some nuclei spin slightly faster (dashed) and others slower (dotted) than the resonance frequency due to local field variations (b). This process continues and leads to a reduction of measurable signal (green line on timeline) along $\boldsymbol{B}_1$ (c). A 180° pulse inverts the magnetization vectors at $t = \frac{1}{2}\mathrm{TE}$ and the spins start to rephase again (d). The total magnetization builds up as the magnetization vectors become in phase (e) and reaches its peak at $t = \mathrm{TE}$ (f). This yields the first echo of the original signal, indicated by the red dot in the timeline.

ing resolution and SNR, one wishes to reduce the scan time by selecting a TR as small as possible that still yields enough signal. However, with a typical 90° pulse the longitudinal magnetization $\boldsymbol{M}_z$ cannot recover sufficiently for very short TR. Thus, the trick is to use low-flip angles which tip only parts of the longitudinal magnetization into the transversal plane such that enough longitudinal magnetization is available for the next repetition after a short TR. The flip angle α of the RF pulse directly controls the resulting magnitude of the transversal magnetization $\|\boldsymbol{M}_{xy}\| = \|\boldsymbol{M}_0\| \sin\alpha$, and the residual longitudinal magnetization $\|\boldsymbol{M}_z\| = \|\boldsymbol{M}_0\| \cos\alpha$, where $\boldsymbol{M}_0$ is the initial magnetization.

Another difference to the spin echo sequence is that GRE uses no 180° refocusing pulse which makes it more susceptible to field inhomogeneities leading to a T_2^* weighting instead of a T_2 weighting.

Also, as there is no 180° pulse, the echo in a GRE sequence is formed via a negative gradient in readout or frequency encoding direction which is an intended dephasing of the magnetization. The idea behind it is that since some time for preparations such as the spatial encoding is needed before the actual signal can be read out, we intentionally delay the time of the peak signal (echo) to a more convenient time. To this end, the dephasing gradient has the inverse sign of the readout gradient and is applied in advance for half of the time of the readout gradient. This ensures that the maximal signal can be obtained at the half of the readout period, since the positive readout gradient reverses the effects of dephasing and recalls the signal during the first half while it gradually dephases again during the second half. This is where the name *gradient recalled echo* stems from.

Yet another characteristic of the GRE sequence is the formation of a *steady state*. In contrast to spin echo sequences, the GRE can have such a short TR that the signal decay due to T_2^* is incomplete and some transversal magnetization remains when the next RF pulse follows. In consequence, transversal magnetization accumulates over a few cycles which is referred to as steady state. As the steady state may be unfavorable for some applications, the so called *spoiled* GRE sequence tries to eliminate the residual transverse magnetization. Otherwise its effects will manifest itself in the image contrast. More on this is subject to further reading [3].

6.4 Advanced Topics

Up to this point, the principles for morphological imaging have been introduced. We will now look at some advanced topics related to speeding up the acquisition process, suppressing signals from unwanted or enhancing signals from desired tissue classes as well as methods for functional imaging.

6.4.1 Parallel Imaging

Long acquisition times are a major drawback of MRI systems, with manifold negative consequences. Patients may experience discomfort, having to spend extended amounts of time in a narrow space. There is an impact on image quality, as patient motion during the acquisition is inevitable. And from a financial standpoint, the amount of MRI examinations per unit time is much less than for other modalities.

Figure 6.11: Parallel imaging uses local receiver coils placed around the patient which capture the signal from multiple positions, allowing for a reduction of acquisition time. The coils are embedded in the table as well as in the flexible coil on top of the patient's chest, in this case an 18-element body coil where individual coil elements are arranged in 6 columns and 3 rows. Three individual coil elements are exemplarily indicated by the red circles. Image courtesy of Siemens Healthineers AG.

Techniques for shortening the acquisition time are, thus, of vital importance and an active field of research. Parallel imaging is an established technique which allows a reduction of the amount of data needed to be acquired in order to reconstruct an image. The name stems from the use of multiple local receiver coils which are placed around the patient and acquire resonance signals in parallel. Modern MRI systems have coil elements which are embedded in the table as well as flexible coil elements which can be placed on the patient (see Fig. 6.11).

This enables many possibilities for undersampling in $\boldsymbol{k}$-space to reduce the acquisition time, one of which we will present here. Suppose we regularly undersample the $\boldsymbol{k}$-space by acquiring only every n-th line. The value n is referred to as the undersampling factor, indicating the reduction in acquisition time. A standard reconstruction by performing a Fourier transform is no longer possible in this case because it will introduce aliasing artifacts in the reconstructed image (see Fig. 6.12).

A reconstruction technique called sensitivity encoding (SENSE) is able to reconstruct an image without aliasing artifacts from such undersampled data by employing the information collected from the multiple receiver coils. It exploits the fact that each local receiver coil "sees" a slightly different image, namely one in which parts closer to the coil are better represented than those

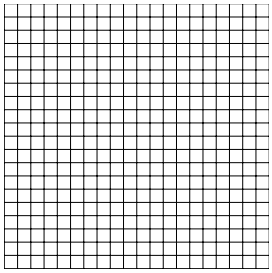

(a) Full sampling

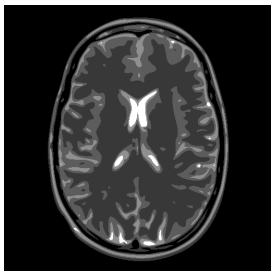

(b) Correct reconstruction

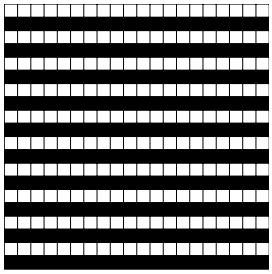

(c) Regular undersampling

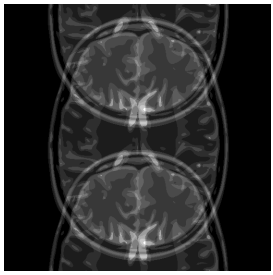

(d) Aliased reconstruction

Figure 6.12: A visualization of a fully sampled $\boldsymbol{k}$-space (a) with its corresponding reconstruction (b) as well as a regularly undersampled $\boldsymbol{k}$-space with every second line missing (c) with a reconstruction showing aliasing artifacts (d).

farther away. A so-called coil sensitivity map $s_\gamma(\boldsymbol{r}_\rho)$ describes how well a coil γ sees a pixel at position $\boldsymbol{r}_\rho$.

In case of regular undersampling, each pixel in the aliased image (see Fig. 6.12(d)) can be described as a weighted sum of several pixels in the unaliased image (see Fig. 6.12(b)). In the given example, 2 pixels in the unaliased image contribute to a pixel in the aliased image. Different local receiver coils "see" different aliased images, where the weights for the weighted sum of pixels are described by the coil sensitivity map of the respective coil. Geek Box 6.3 illustrates this for an idealized 2-coil setup whereas Geek Box 6.4 discusses how to calibrate the sensitivity maps online.

Geek Box 6.3: Coil Sensitivity Maps

The parallel measurement can be described by a linear system of equations:

$$\boldsymbol{a} = \boldsymbol{S}\boldsymbol{v}, \tag{6.9}$$

where $\boldsymbol{v}$ is a vector of length m of unaliased pixel values contributing to an aliased pixel, $\boldsymbol{a}$ is a vector of length c of the aliased pixel value as seen by the c different coils and $\boldsymbol{S}$ is a $c \times m$ matrix containing the coil sensitivities as

$$\boldsymbol{S}_{\gamma,\rho} = s_\gamma(\boldsymbol{r}_\rho), \tag{6.10}$$

where γ is the coil index and $\boldsymbol{r}_\rho$ are the pixel positions of the pixels contained in $\boldsymbol{v}$. The reconstruction then consists of solving Eq. (6.9) for all pixels in the unaliased image.

This process can be visualized looking at idealized coil sensitivity maps for a 2-coil setup where one coil is more sensitive in the upper part of the image and the other in the lower part of the image:

Sensitivity map of Coil 1

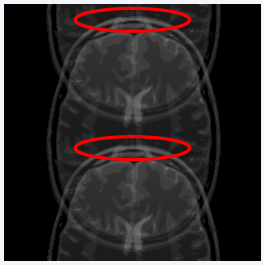

Aliased image of Coil 1

Sensitivity map of Coil 2

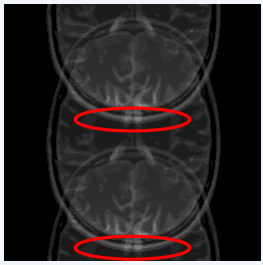

Aliased image of Coil 2

Here, brighter values represent higher weights. The aliased images seen by these coils differ, one has a better representation of the top part of the head and one a better representation of the bottom part, see the red highlights.

Geek Box 6.4: Coil Sensitivity Map Calibration

A remaining problem is how to compute the coil sensitivity maps. An a-priori calibration is infeasible as they are dependent on the imaging volume. Therefore, we describe an *auto-calibration* approach can be used to determine coil sensitivity maps during the scan.
In addition to the undersampled acquisition as shown in Fig. 6.12(c), a small, fully sampled region around the center of $\boldsymbol{k}$-space is measured. A direct Fourier transform reconstruction of this region for each coil leads to low-resolution versions of the volume as seen by the respective coil, for our two-coil example:

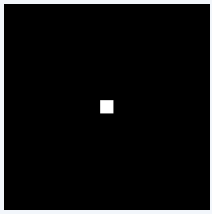
Acquisition mask

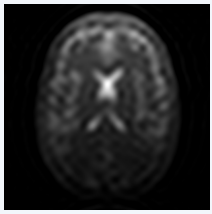
Image of Coil 1

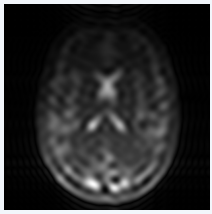
Image of Coil 2

An approximation of the coil sensitivity maps is obtained by dividing these images by a sum-of-squares combination of all coil images:

$$s_\gamma(\boldsymbol{r}_\rho) = \frac{i_\gamma(\boldsymbol{r}_\rho)}{\sqrt{\sum_{\gamma'=1}^{C} i_{\gamma'}(\boldsymbol{r}_\rho)^2}}, \tag{6.11}$$

where $i_\gamma(\boldsymbol{r}_\rho)$ is the image of coil γ and C is their total number:

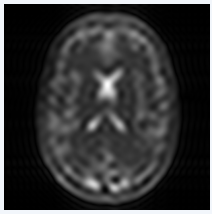
Fusion of Coil 1 and 2
$\sqrt{\sum_{\gamma'=1}^{C} i_{\gamma'}(\boldsymbol{r}_\rho)^2}$


Sensitivity Map 1
$s_1(\boldsymbol{r}_\rho)$


Sensitivity Map 2
$s_2(\boldsymbol{r}_\rho)$

The resulting coil sensitivity maps show artifacts in the regions with little to no signal as compared to the idealized maps. Reconstructions using these coil sensitivity maps will display noise amplification in air regions due to these artifacts. More advanced methods exist to deal with these issues, but they are beyond the scope of this text.

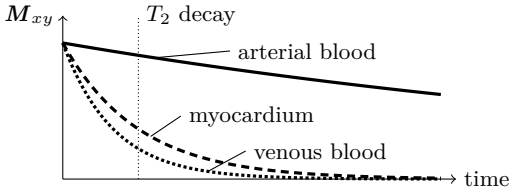

Figure 6.13: A T_2 preparation sequence can be used to increase the contrast between myocardium and arterial blood due to their large difference in T_2 constants (35 ms vs. 250 ms). Figure recreated from [6].

6.4.2 Spectrally Selective Excitation

For bright-blood coronary imaging, it is often desirable to increase contrast between the myocardium (the heart muscle) and the arterial blood within the heart chambers. This allows a better delineation of the heart walls and thus increases the diagnostic value of images. A method called T_2 preparation exploits the fact that arterial blood has a much larger T_2 constant than myocardial tissue and venous blood. This means that the decay of transversal magnetization $\boldsymbol{M}_{xy}$ is slower for arterial blood, see Fig. 6.13.

Using a sequence of pulses, we can reduce the magnetization of the myocardium and venous blood while keeping the magnetization of arterial blood virtually untouched. Fig. 6.14 illustrates the process. In the initial state, spins of all tissue types are aligned with the main magnetic field $\boldsymbol{B}_0$. A 90° pulse pushes the spins into the transversal plane, where they precess. At this point, T_1, T_2 and T_2^* relaxation (see Sec. 6.1.2) start to affect the spins:

$\boldsymbol{T_1}$ relaxation: We will ignore T_1 relaxation here because it happens on a much larger timescale than the duration of the T_2 preparation sequence.

$\boldsymbol{T_2^*}$ relaxation: Due to magnetic field inhomogeneities, spins would rapidly dephase and lose their transversal magnetization, known as T_2^* relaxation. To counteract this effect, we apply a series of 180° pulses to refocus the spins.

$\boldsymbol{T_2}$ relaxation: This is the effect we actually want to happen. While the spins remain in the transversal plane, myocardium and venous blood spins lose their transversal magnetization much faster than arterial blood.

After a set amount of time, a final −90° pulse realigns spins with the main magnetic field. At this point, arterial blood spins have a higher magnetization and subsequent imaging sequences (e. g., GRE or spin echo sequences) will show an increased contrast to myocardial tissue.

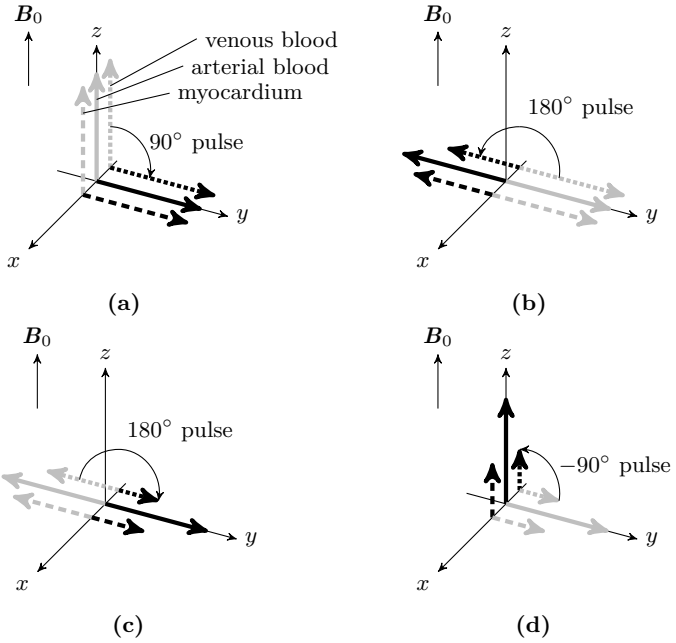

Figure 6.14: In the initial state, the spins for myocardial tissue, venous and arterial blood are all aligned along the main magnetic field. A 90° pulse pushes them into the xy plane, where they precess (a). 180° refocusing pulses are used to counteract T_2^* relaxation, so only T_2 relaxation affects the spins while they are in the xy plane (b), (c). Due to the different T_2 constants, the transversal magnetization decays faster for myocardial and venous blood spins. After a set amount of time, spins are realigned with the main magnetic field by a −90° pulse (d). An imaging sequence following this preparation sequence will now display increased contrast between arterial blood and myocardial tissue. Figure recreated from [6].

6.4.3 Non-contrast Angiography

Up to this point, we have quietly assumed that all measured spins remain stationary for the duration of the imaging. This assumption is, of course, invalid if we image the human body. For many applications, we have to adapt the acquisition protocol to minimize artifacts due to motion. For example, we may ask the person being scanned to hold their breath to minimize respiratory motion artifacts. Imaging sequences with a short TR can be used to "freeze" cardiac motion. But in some cases, we can actually use non-stationary spins to our advantage.

Angiography, the imaging of blood vessels, is commonly performed by administering a contrast agent which increases the contrast of blood to sur-

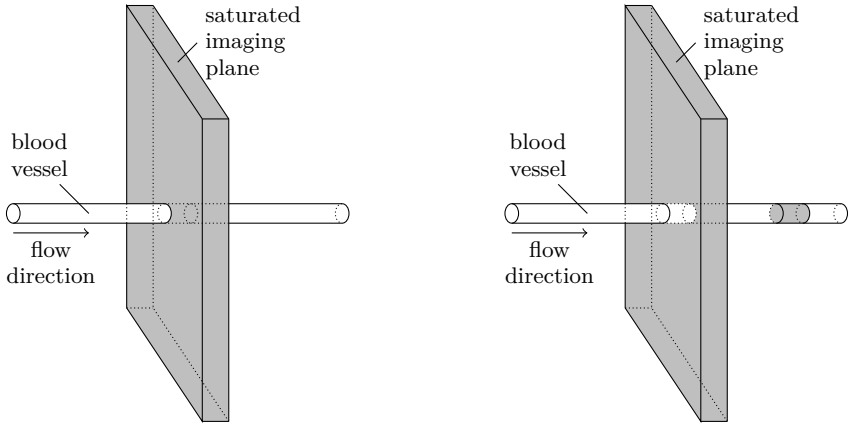

(a) Directly after saturation

(b) Unsaturated spins enter the imaging plane due to blood flow

Figure 6.15: For non-contrast TOF angiography, all spins in the desired imaging plane are saturated, i. e., put in a state such that they cannot be excited by an RF pulse, indicated by the gray shading (a). Due to blood flow, unsaturated spins enter the imaging plane for blood vessels that are not entirely parallel to the imaging plane (b). Subsequent imaging sequences will show a high contrast between those vessels and surrounding stationary tissue.

rounding tissues. In MRI, we can use the fact that blood spins move continuously during the image acquisition to perform a non-contrast angiography. In the magnetic resonance context, the TOF effect refers to the short amount of time that flowing blood spins remain within an imaging slice.

For TOF angiography, we first saturate all spins within our imaging plane, i. e., put them in a state where they cannot be excited by an RF pulse. For the duration of their T_1 relaxation, stationary spins within the imaging plane will thus show little to no signal if we perform an imaging sequence. But due to the TOF effect, unsaturated blood spins continuously flow into the imaging plane and will appear bright in contrast to the surrounding stationary tissue if imaged.

This imaging technique works best for blood vessels perpendicular to the imaging plane. For vessels that lie within the imaging plane, the contrast becomes weaker with increasing distance to the point where unsaturated spins enter the imaging plane. Fig. 6.15 illustrates the concept of TOF angiography.

6.4.4 The BOLD Effect

One of the applications of functional magnetic resonance imaging (fMRI) is the visualization of neuronal activity in the brain. Increased neuronal activity leads to local oxygen depletion in the active regions of the brain. This lack of oxygen is subsequently overcompensated, leading to a higher concentration of oxygenated blood in the active regions. Thus, an increased oxygen concentration can be seen as an indication of neuronal activity.

Our aim is to measure this increased concentration using the blood-oxygenation-level dependent (BOLD) effect, which describes the different magnetic properties of oxygenated and deoxygenated hemoglobin. Blood containing higher concentrations of oxygenated hemoglobin has a higher T_2^* constant, i. e., less dephasing due to local magnetic field inhomogeneity (see Sec. 6.1.2). Thus, to measure the neuronal activity due to an external stimulus, we can compare images acquired in a resting state to images acquired during the application of the stimulus to see which brain regions experience a change in local oxygen concentration.

A GRE sequence (see Sec. 6.3) can be used to obtain T_2^* weighted images. However, as the T_2^* differences are very slight, the usual approach to gain robust results is to acquire multiple resting state images and multiple images while the stimulus is applied in an alternating fashion, followed by a statistical test to determine if the intensity of a given pixel significantly differs in both sets of images.

Further Reading

[1] Christoph Forman et al. “Free-Breathing Whole-Heart Coronary MRA: Motion Compensation Integrated into 3D Cartesian Compressed Sensing Reconstruction”. In: *MICCAI 2013, Part II, LNCS 8150*. Ed. by K. Mori et al. Nagoya, Japan, 2013, pp. 575–582.

[2] Lars G Hanson. *Introduction to Magnetic Resonance Imaging Techniques*. Tech. rep. Danish Research Centre for Magnetic Resonance, 2009. URL: http://eprints.drcmr.dk/37/.

[3] R.H. Hashemi, W.G. Bradley, and C.J. Lisanti. *MRI: The Basics*. Lippincott Williams & Wilkins, 2010. ISBN: 9781608311156.

[4] Alexander Hendrix. *Magnets, Flows and Artifacts: Basics, Techniques, and Applications of Magnetic Resonance Tomography*. Siemens AG, Erlangen, 2004. URL: http://www.healthcare.siemens.de/magnetic-resonance-imaging/magnetom-world/publications/mr-basics.

[5] Alexander Hendrix. *Magnets, Spins and Resonances: An introduction to the basics of Magnetic Resonance*. Siemens AG, Erlangen, 2003. URL: http://www.healthcare.siemens.de/magnetic-resonance-imaging/magnetom-world/publications/mr-basics.

[6] Vivian S Lee. *Cardiovascular MRI: Physical Principles to Practical Protocols*. Lippincott Williams & Wilkins, Dec. 2005. ISBN: 0781779960.

[7] Dwight G Nishimura. *Principles of Magnetic Resonance Imaging*. Self-published, 2010. URL: http://www-ee.stanford.edu/~dwight/book.html.

[8] Klaas P Pruessmann et al. "SENSE: sensitivity encoding for fast MRI". In: *Magn Reson Med* 42.5 (Nov. 1999), pp. 952–962.

[9] G. Lawrence Zeng. *Medical Image Reconstruction: A Tutorial*. Higher Education Press, Springer, Beijing, 2009. ISBN: 978-3-642-05367-2.